Applied Surface Science 619 (2023) 156714

Contents lists available at ScienceDirect

Applied Surface Science

journal homepage: www.elsevier.com/locate/apsusc

Full Length Article

Mesoporous Co_3O_4 nanosheets with exposed Co^{2+}-rich crystal facets for improved toluene detection

Dehao Kong [a], Weirong Zhou [a], Jiayin Han [a], Yubing Gao [a], Yuan Gao [a,*], Liupeng Zhao [a], Peng Sun [a,b,*], Geyu Lu [a,b]

[a] State Key Laboratory on Integrated Optoelectronics, Key Laboratory of Advanced Gas Sensors of Jilin Province, College of Electronic Science and Engineering, Jilin University, 2699 Qianjin Street, Changchun, Jilin Province 130012, People's Republic of China
[b] International Center of Future Science, Jilin University, 2699 Qianjin Street, Changchun, Jilin Province 130012, People's Republic of China

ARTICLE INFO

Keywords:
Crystal facet engineering
Co_3O_4 mesoporous nanosheet
Multivalence
Toluene sensor
Activation energy

ABSTRACT

Crystal facet engineering strategy is an effective way to regulate the exposed facets, which affect the ability of the surface to adsorb and react with gas molecules, ultimately enhancing the gas-sensing properties. In this work, Co_3O_4 mesoporous nanosheets with dominant exposed {1 1 1} facets (Co_3O_4-60) or {1 1 2} facets (Co_3O_4-100) were synthesized by simply adjusting the condensation-reflux temperature. The sensing results toward toluene show that Co_3O_4-60 exhibited superior performance. According to the crystal structure analysis and work function calculations, the (1 1 1) facet composed of Co^{2+} would adsorb more oxygen molecules, which have been proved by experimental characterization, facilitating the sensing efficiency. The results of X-ray photoelectron spectroscopy indicated that Co_3O_4-60 possesses a higher Co^{2+} content and chemisorbed oxygen ratio (52.9%). Furthermore, Co_3O_4-60 has a high electrical conductivity and a minor apparent activation energy for toluene (38.75 kJ/mol). The gas sensor based on Co_3O_4-60 exhibited a response of 20.6 for 100 ppm toluene with rapid recovery and a detection limit of 1 ppm. Besides, other properties such as selectivity, repeatability, and humidity resistance were evaluated. This work evidences that crystal facet engineering is a practical approach to improving the gas-sensing properties of pure-phase Co_3O_4.

1. Introduction

Toluene is a representative volatile organic compound (VOC) that has a unique aromatic odor. Toluene can be used as a solvent in the synthesis of oil, rubber, and asphalt, and it is also the primary raw material for producing many dyes [1]. Toluene is highly irritating and anesthetic [2], while prolonged exposure can cause symptoms such as headaches, nausea, anorexia, and damage to the human liver and brain [3]. The permissible concentration-time weighted average (PC-TWA) of toluene is 50 mg/m^3 (~12 ppm) according to the Chinese regulation (GBZ2.1-2019). Therefore, developing gas sensors with real-time and accurate monitoring of toluene is of great importance to protect human health and ensure safe production.

Chemiresistive gas sensors based on metal oxide semiconductors (MOSs) have the advantages of small size, high sensitivity, and short response time [4], making them ideal for toluene detection. Recently, many studies have used doping [5], heterostructure design [6], noble metal loading [7], or other means to further improve the gas-sensing properties of MOSs to toluene but underestimate the influences of crystal facets. Engineering the exposed crystal facets could regulate the atomic configuration of the surface to fully expose the expected chemical state, bonding, and vacancies, significantly impacting the gas sensing performance [8,9]. For instance, Xu et al. prepared ZnO nanosheets with exposed (0 0 0 1) or (1 0 $\bar{1}$ 0) facets [10]. The ZnO nanosheets with exposed (0 0 0 1) facets demonstrated better ethanol detection due to the abundance of unsaturated dangling bonds and oxygen vacancy defects.

Cobalt (II, III) oxide (Co_3O_4) is a p-type MOS with multivalence that commonly exhibits high catalytic activity towards toluene [11]. Meanwhile, its variable oxidation state facilitates the adsorption of reactive surface oxygen at relatively low temperatures [12,13], which contributes to the process of toluene sensing. Therefore, in addition to the crystal facet alteration, Co^{2+} and Co^{3+} in Co_3O_4 would also play different roles in gas sensing [14]. Although no research shows the

* Corresponding authors at: State Key Laboratory on Integrated Optoelectronics, Key Laboratory of Advanced Gas Sensors of Jilin Province, College of Electronic Science and Engineering, Jilin University, 2699 Qianjin Street, Changchun, Jilin Province 130012, People's Republic of China.
E-mail addresses: gaoyuan@jlu.edu.cn (Y. Gao), pengsun@jlu.edu.cn (P. Sun).

https://doi.org/10.1016/j.apsusc.2023.156714
Received 11 January 2023; Received in revised form 3 February 2023; Accepted 8 February 2023
Available online 11 February 2023

optimal ratio of Co^{2+} to Co^{3+} for gas detection, relevant literature has reported that higher Co^{2+} content could improve gas sensing performance [15,16]. Further combined with its crystal structure in Fig. S1, the (1 1 1) facet of Co_3O_4 is composed entirely of tetrahedral Co^{2+} cations. Therefore, preparing Co_3O_4 with dominant exposed {1 1 1} facets is significant for us to explore the role of crystal facets and prepare toluene sensors.

In this work, we synthesized Co_3O_4 nanosheets with exposed Co^{2+}-rich crystal facets using a facile and controllable condensation-reflux method combined with post-calcination treatment. The formation of CoOOH intermediate would induce the transition between the exposed {1 1 1} facets and the {1 1 2} facets of Co_3O_4 [17]. The exposed facets {1 1 1} guaranteed fertile Co^{2+} and chemisorbed oxygen available on the large surface of nanosheets, which promote the gas sensing synergistically. The gas sensor based on Co_3O_4-60 (with exposed {1 1 1} facets) had a gas response of 20.6 for 100 ppm toluene at its optimum operating temperature of 170 °C, which was over three times that of Co_3O_4-100 with exposed {1 1 2} facets (180 °C, 6.5). Also, it exhibited a lower baseline resistance, rapid recovery time, and remarkable selectivity, contributing to its practical application.

2. Experimental section

2.1. Chemical synthesis

The Co_3O_4 mesoporous nanosheets were prepared by condensation-reflux combined with calcination treatment [17]. The schematic diagram of $Co(OH)_2$ precursors synthesis was shown in Scheme 1. Cobalt nitrate hexahydrate (99%, $Co(NO_3)_2{\cdot}6H_2O$) and 2-Methylimidazole (98%, $C_4H_6N_2$) were purchased from Shanghai Aladdin Biochemical Technology Co., LTD., and were not further purified in use. Typically, 1 mmol $Co(NO_3)_2{\cdot}6H_2O$ was mixed with 50 ml deionized water and stirred until a homogeneous solution was formed. Subsequently, 8 mmol 2-Methylimidazole was added to the above aqueous solution, and stirring was continued until complete dissolution. The mixed solution was refluxed for 1 h at 60 °C, 80 °C, and 100 °C, respectively, to precipitate the precursor $Co(OH)_2$-T (T represents the reaction temperature, 60, 80, or 100). The precursors were centrifuged, washed with water four times, and placed into a vacuum drying oven of 80 °C. After thoroughly drying, these precursor powders were calcinated in a muffle furnace at 350 °C for 2 h with a heating rate of 2 °C/min to obtain Co_3O_4-T.

2.2. Characterization instruments

X-ray diffraction (XRD, Rigaku D/Max-2550, 10-80°) and Raman spectra (RENISHAW INVIA Micro-Raman spectrometer, excitation wavelength 532 nm, 100–1200 cm^{-1}) characterized the materials' composition and crystal structure. Field emission scanning electron microscope (FESEM/SEM, JEOL JSM-7500F) and transmission electron microscope (TEM, JEOL JEM-2200FS) jointly characterized their morphology. The exposed crystal facets were analyzed using a high-resolution transmission electron microscope (HRTEM) and selected area electron diffraction (SAED). The specific surface area and pore size were obtained by Brunauer-Emmett-Teller test (Micromeritics Gemini VII2390) and combined with Barrett-Joyner-Halenda analysis. Their work functions were compared by Kelvin probe (KP 6500 Digital Kelvin Probe McAllister Technical Services Co., Ltd.). X-ray photoelectron spectroscopy (XPS, PREVAC XPS system) analyzed the surface elements and valence states of these samples. Binding energies have been calibrated by the C 1s peak (284.8 eV). And the same feature of different samples has approximately the same full width at half maximum (FWHM) in the fits.

2.3. Manufacturing and testing of gas sensors

The sensor structure is shown in Fig. S2a. First, an appropriate amount of Co_3O_4 powder was placed in an agate mortar and lightly ground while dropping deionized water until a paste was formed. Then, it was quickly applied to the surface of ceramic tubes. It can be seen from Fig. S2b and Fig. S2c1-c3 that the sensor film uniformly covered the ceramic tube with an approximate thickness of 25 μm. The ceramic tubes coated with sensing materials were treated at 250 °C for 2 h to enhance their adhesion. Then, after passing through a Ni-Cr alloy heating coil (~38 Ω), the four wires of the ceramic tube and the two ends of the heating coil were welded to a hexagonal tube base to construct a gas sensor. The Joule heat of the Ni-Cr heating coil could regulate the sensor's operating temperature. Three of each sensor were prepared and tested to evaluate their deviation.

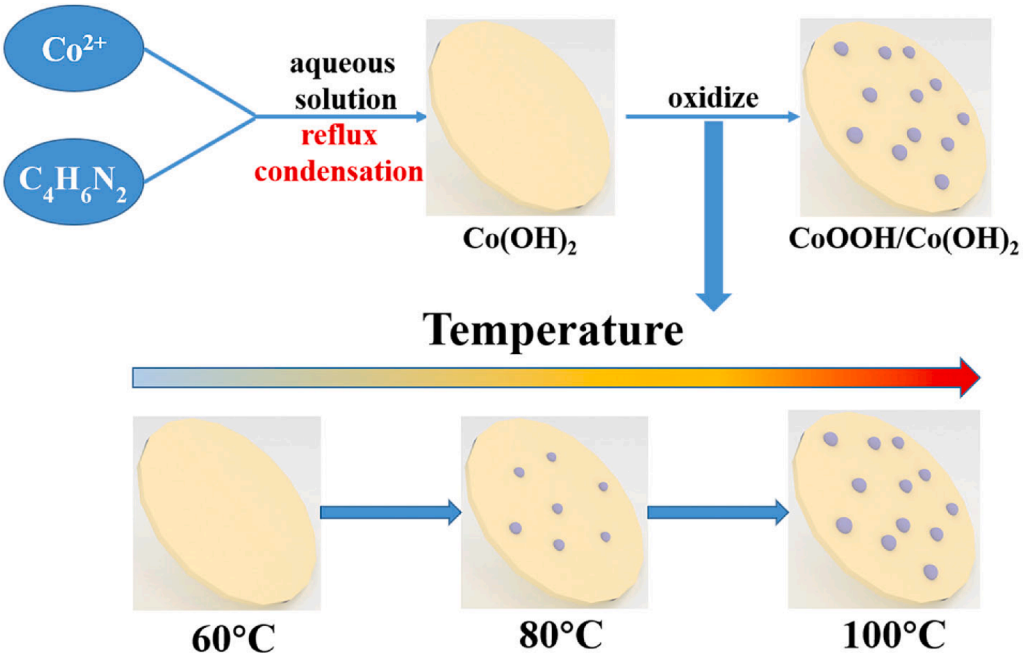

Scheme 1. The illustration for the $Co(OH)_2$ precursors synthesis.

A static system shown in Fig. S3 was used to test the gas sensing properties. A digital multimeter recorded the sensors' resistance at one-second intervals. The gas sensor was initially in an air chamber (1 L) filled with ambient air to obtain its baseline resistance (R_a). Then, the sensor was transferred to a chamber containing the test gas to obtain its gas resistance (R_g), and finally, it was placed back into the air chamber to recover the resistance. Therefore, the gas response is defined as $S = R_g/R_a$. It is generally considered that effective detection of the target gas can be achieved when $S > 1.2$. Moreover, response time and recovery time are typically considered to be the time it takes for a sensor to respond or recover to 90%. It is worth noting that the transfer between chambers is done in less than one second; thus, considering the response and recovery rates of the sensors in this work, the effect of resistance fluctuations during this process on the response-recovery time and apparent activation energy calculation is considered negligible.

These sensors were placed in advance in the experimental environment (24 ± 2 °C, 15 ± 3RH%) and aged at an operating temperature of 170 °C for two days to stabilize the following tests. A humidity chamber with a constant temperature of 25 °C controlled humidity regulation during the moisture effect test.

More details about the gas configuration were placed in the Supplementary Material.

3. Results and discussion

3.1. Characterization of materials

The $Co(OH)_2$ precursors were obtained after condensation-reflux. The XRD patterns of the precursors obtained at different reflux temperatures are shown in Fig. 1a. All the precursors are in good agreement with the typical β-$Co(OH)_2$ (JCPDS No. 74-1057). Moreover, the Raman spectra of these $Co(OH)_2$ precursors are characterized in Fig. 1b. The peak at 690 cm^{-1} emerges gradually with the rise of reflux temperature. The new peak is attributed to the spinel structure Co_3O_4. It has been reported that CoOOH undergoes a phase transition when irradiated by a laser higher than 10 mW [18,19]. Fig. 1c–e show the SEM images of Co$(OH)_2$ obtained at different reflux temperatures. All the precursors are circular nanosheets, but with smaller sizes, rougher surfaces, and jaggier edges when prepared at higher reflux temperatures. The nanosheet diameter dropped from nearly 4 μm (Co_3O_4-60) to less than 3 μm (Co_3O_4-100). This phenomenon further validates the formation process of CoOOH. As the reflux temperature increased, the protons generated by Co^{2+} hydrolysis would etch the edges of the $Co(OH)_2$ nanosheets formed in the preliminary step. Parts of the released metal ions were oxidized at high temperatures and then reacted with hydroxyl groups generated by the protonation of 2-Methylimidazole in the aqueous solution to form CoOOH. Thus, we inferred the existence of CoOOH intermedia in the $Co(OH)_2$ precursors obtained at higher reflux temperatures (80 and 100 °C).

The XRD patterns of the calcinated samples are shown in Fig. 2a. The materials are all cubic phase Co_3O_4 (JCPDS NO. 43-1003), indicating the complete conversion of $Co(OH)_2$ at 350 °C. The crystallites size and strain of the samples were calculated using Williamson-Hall (W-H) method:

$$\beta\cos\theta = K\lambda/D + 4\varepsilon\sin\theta \quad (1)$$

where β is the FWHM of the diffraction peak, θ is the peak position in radians, λ = 0.15418 nm is the wavelength of X-ray, K = 0.9 is the shape factor, D is the crystallite size, and ε is the lattice strain. Therefore, the crystallite size and the lattice strain can be given by the intercept and the slope of the linear fitted βcosθ ~ 4sinθ shown in Fig. S4. These data are summarized in Table S1. The crystallite size of Co_3O_4-60 is 27.9 nm, which is bigger than that of Co_3O_4-80 (20.9 nm) and Co_3O_4-100 (17.2 nm). The charge transport in polycrystalline materials is mainly influenced by grain boundary effects [20], where more grain boundaries between small crystallites reduce their carrier mobility. Besides the largest crystallite size, Co_3O_4-60 also has the hugest lattice stretching strain, which may imply more defect sites, such as oxygen vacancies [21,22]. Five peaks of $F_{2g}^{(1)}$, E_{2g}, $F_{2g}^{(2)}$, $F_{2g}^{(3)}$, and A_{1g} can be observed in the Raman characterization (Fig. 2b) which proves their spinel structure [23]. The morphologies of Co_3O_4 are characterized by the SEM images in Fig. 2c-e. The calcination did not damage the nanosheets, but some cracks appeared due to the decomposition of the precursors. Further, the nitrogen adsorption-desorption isotherms and corresponding pore-size distributions of the samples were tested as in Fig. S5. Compared with Co_3O_4-60 (37.2 m^2/g) and Co_3O_4-80 (35.8 m^2/g), the higher specific surface area of Co_3O_4-100 (45.1 m^2/g) is attributed to its rougher nanosheet edges and surface-dispersed nanoparticles. Meanwhile, the three Co_3O_4 nanosheets have similar mesopore size distributions (~12.5 nm), which facilitates the diffusion and infiltration of gases within the material. The results show that Co_3O_4-60 does not have the biggest surface area but superior sensing properties, which indicates the surface area did not dominate the sensing properties in our case.

The pores are proved again by the TEM images of Fig. 3a and 3d. The

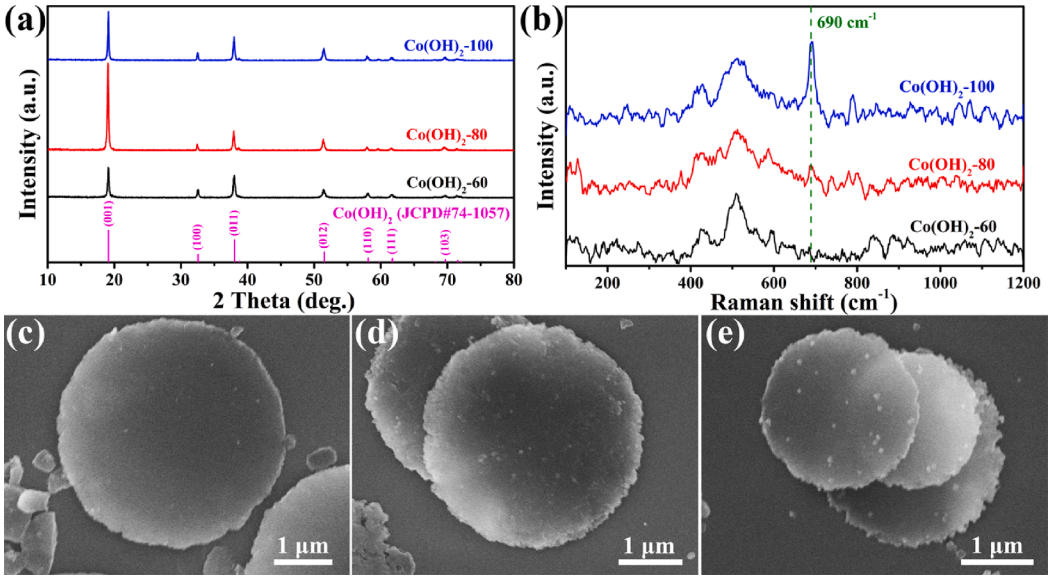

Fig. 1. (a) XRD patterns and (b) Raman spectra of $Co(OH)_2$ precursors; SEM images of (c) $Co(OH)_2$-60, (d) $Co(OH)_2$-80 and (e) $Co(OH)_2$-100.

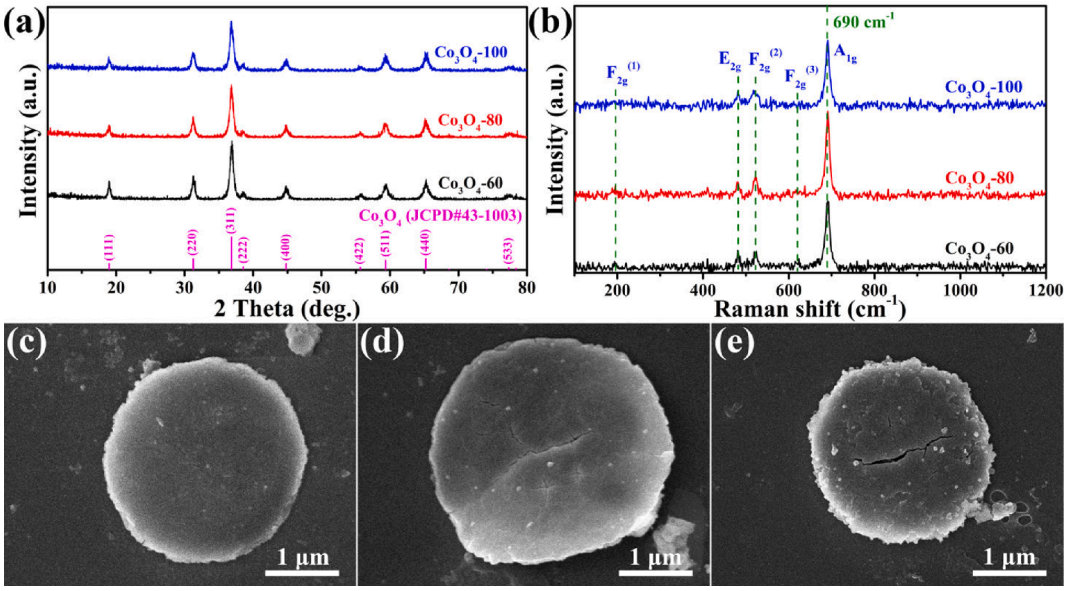

Fig. 2. (a) XRD patterns and (b) Raman spectra of Co_3O_4 nanosheets; SEM images of (c) Co_3O_4-60, (d) Co_3O_4-80 and (e) Co_3O_4-100.

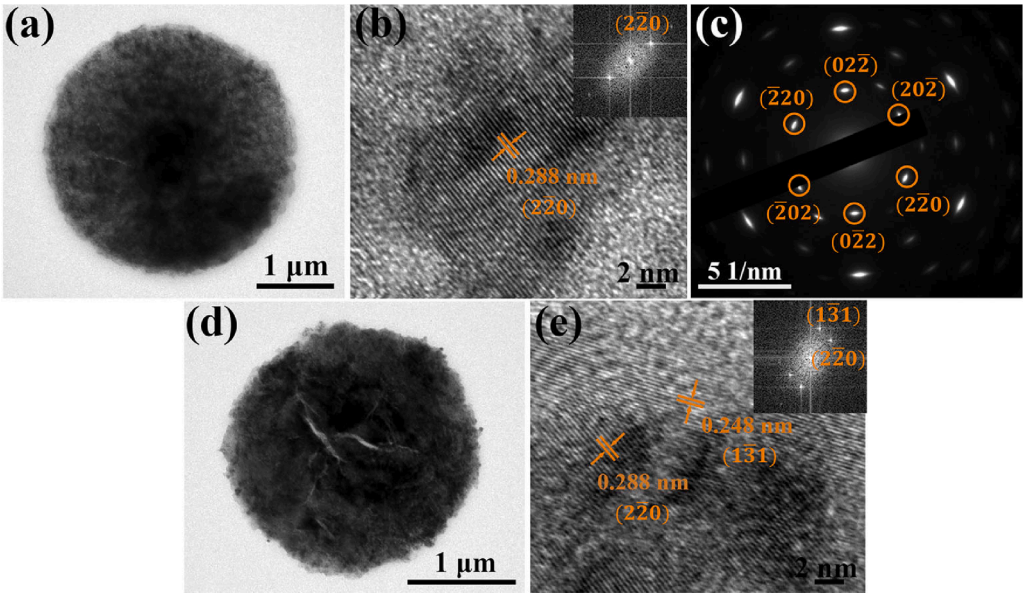

Fig. 3. TEM and HRTEM (FFT) images of (a, b) Co_3O_4-60 and (d, e) Co_3O_4-100; (c) the SAED image of Co_3O_4-60.

HRTEM image of Co_3O_4-60 (Fig. 3b) reveals the lattice spacing of 0.288 nm, which corresponds to the (2$\bar{2}$0) atomic plans. Furthermore, the SAED of Fig. 3c shows the interface angle of 60°, and the six diffraction points could be allocated to ($\bar{2}$20), (02$\bar{2}$), (20$\bar{2}$), (2$\bar{2}$0), (0$\bar{2}$2), and ($\bar{2}$02). These characteristics demonstrate that {1 1 1} facets are the dominant exposed crystal facets of Co_3O_4-60 [24]. Meanwhile, the HRTEM and

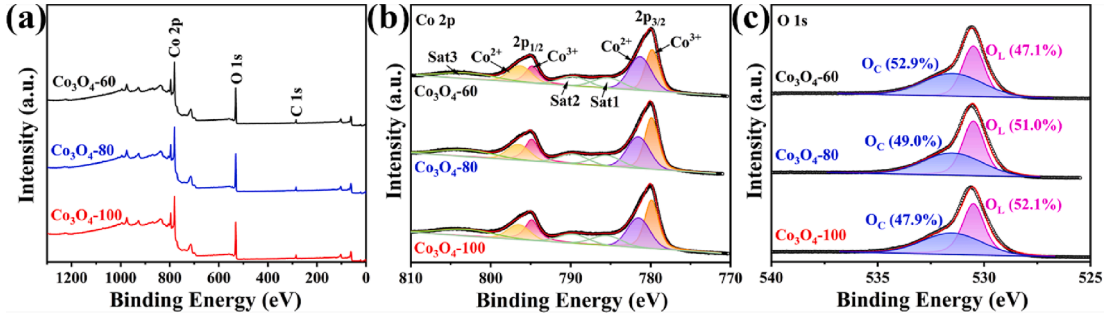

Fig. 4. (a) XPS survey, (b) Co 2p and (c) O 1s spectra of Co_3O_4 nanosheets.

corresponding fast Fourier transform (FFT) pattern (inset) of Co_3O_4-100 were shown in Fig. 3e. The exposed (2$\bar{2}$0) and (1$\bar{3}$1) atomic plans reveal that the dominant exposed crystal facets of Co_3O_4-100 have transformed into {1 1 2} facets because of the intervention of CoOOH [17,25]. The (1 1 1) facet compose entirely of Co^{2+}, which possesses a higher Co^{2+} ratio compared with the (1 1 2) facet (Fig. S1).

The element composition and chemical state on the surface of the Co_3O_4 materials were analyzed by XPS and illustrated in Fig. 4, where Fig. 4a-c are the XPS survey, Co 2p, and O 1s spectra, respectively. The element composition ratios can be determined by the integrated peak areas of individual ones. In Fig. 4b, the binding energies of the two peaks at ~795 eV and ~780 eV correspond to Co $2p_{1/2}$ and Co $2p_{3/2}$, while the other three contributions of the Co 2p spectra are attributed to satellite peaks (Sat1, Sat2, and Sat3) [25,26]. The details of the constraints on the Co 2p spectra fits are as follows: the peaks representing the same cations (Co^{2+} or Co^{3+}) in $2p_{1/2}$ and $2p_{3/2}$ have equal FWHM and determined relative intensity (1:2), the FWHM of the two narrower satellite peaks (Sat1 and Sat2) are equal, the FWHM of the largest satellite peak (Sat3) is constant at 8 eV, and their tail heights are all the same [27]. Accordingly, Co $2p_{1/2}$ and Co $2p_{3/2}$ were deconvoluted into two peaks of Co^{2+} (~796.5 eV and ~781.5 eV) and Co^{3+} (~794.9 eV and ~779.9 eV), respectively. For both two cations, the difference between Co $2p_{1/2}$ and Co $2p_{3/2}$ was as the same as 15.0 eV. Then, the ratio of Co^{2+} to Co^{3+} (Co^{2+}/Co^{3+}) was calculated. Co_3O_4-60 has the highest Co^{2+}/Co^{3+} (1.23), which is significantly greater than that of Co_3O_4-80 (0.86) and Co_3O_4-100 (0.83). And this may be related to the exposed crystal facets [25]. The Co^{2+} in Co_3O_4 has higher catalytic activity [28], which should be beneficial to promoting the reaction of gases on the surface during the sensing. Meanwhile, higher Co^{2+}/Co^{3+} usually means more oxygen vacancies are generated on the surface [29], and the oxygen vacancies can trap and activate gaseous oxygen molecules to form surface chemisorbed oxygen [30]. The binding energy of the O 1s spectra in Fig. 4c is located at 530.6 eV, which could be further deconvoluted into two peaks representing lattice oxygen (O_L, ~530.5 eV) and chemisorbed oxygen (O_C, ~531.5 eV) [31]. The content of chemisorbed oxygen was calculated by curve fitting area ratio of $O_C/(O_C + O_L)$, and the results are 52.9% (Co_3O_4-60), 49.0% (Co_3O_4-80), and 47.9% (Co_3O_4-100), respectively. Co_3O_4-60 has the most chemisorbed oxygen, and the content of chemisorbed oxygen gradually decreases with the increase of reflux temperature, which is consistent with the trend of Co^{2+}/Co^{3+}. This phenomenon is further demonstrated by the Fermi level changes (Fig. S6) measured by Kelvin probe. More chemisorbed oxygen led to more electron loss from the conduction band, which caused greater energy band bending and ultimately resulted in the largest work function of Co_3O_4-60. It is widely recognized that chemisorbed oxygen directly participates in the process of gas-sensing reaction. More chemisorbed oxygen provides convenient reaction kinetics, which is essential to improve gas-sensing performance.

3.2. Toluene sensing properties

The Co_3O_4 samples were made into gas sensors. Their baseline resistance in the operating range of 110–200 °C is shown in Fig. 5a. The baseline resistance decreases with increasing operating temperature, which verifies their semiconducting properties [32]. Meanwhile, the sensor based on Co_3O_4-60 exhibits lower baseline resistance at the same operating temperature. The I-V curves of the devices were further tested at 170 and 180 °C as Fig. 5b-c, where their conductivity showed the same trend as the device resistance. And these straight I-V curves also demonstrate an excellent ohmic contact between the sensitive material and the electrodes. Furthermore, Fig. 6 and Fig. S7 summarizes each sensor's gas response and response-recovery curves to 100 ppm toluene over the operating temperature range of 110–200 °C, respectively. The response of each sensor shows a "volcanic" trend that rises and then falls with increasing operating temperature because the sensors' optimal operating temperature is jointly determined by the reactivity and adsorption-desorption capacity of gas molecules. The gas sensor based on Co_3O_4-60 confirmed its lowest baseline resistance (20.4 kΩ) and highest response (20.6 for 100 ppm toluene) at a low optimum operating temperature (170 °C), outperforming those gas sensors based on Co_3O_4-80 (60.8 kΩ, 9.3, 180 °C) and Co_3O_4-100 (512.3 kΩ, 6.5, 180 °C).

The response of each gas sensor to 100 ppm of different VOCs, containing triethylamine, toluene, acetone, ethanol, formaldehyde, and methanol, is shown in Fig. S8. The Co_3O_4-60 gas sensor exhibits the lowest optimum operating temperature for all the tested VOCs. This general variation trend originates from the adsorbed oxygen species on the Co_3O_4-60. Moreover, the lowest operating temperature indicates that the least activation energy is required for the gas-sensing reaction, which involves the surface reaction occurring during the sensing process. The Arrhenius equation was used to calculate the apparent activation energy (E_{aa}), and the method was detailed in the supplementary material [33]. The baseline resistances at different temperatures have been normalized before conversion to ensure consistency of comparison. Fig. 7a-c show the resistance changes of Co_3O_4-60, Co_3O_4-80, and Co_3O_4-100 to 100 ppm toluene at different operating temperatures and were converted into Arrhenius-type plots between resistance change

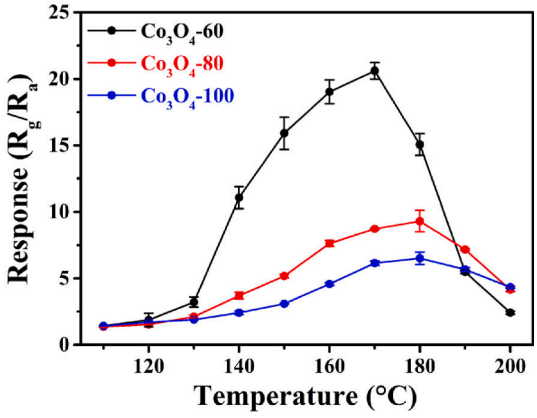

Fig. 6. Responses of the sensors to 100 ppm toluene at different operating temperatures.

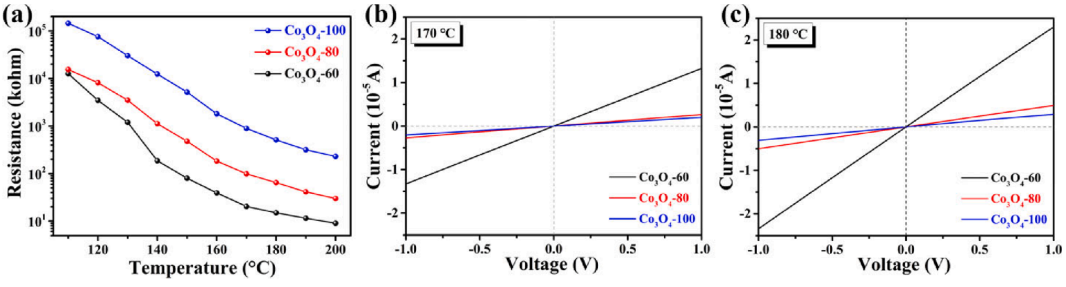

Fig. 5. (a) The dependence between the resistance of the sensors and the operating temperature; and the I-V curves at (b) 170 °C and (c) 180 °C.

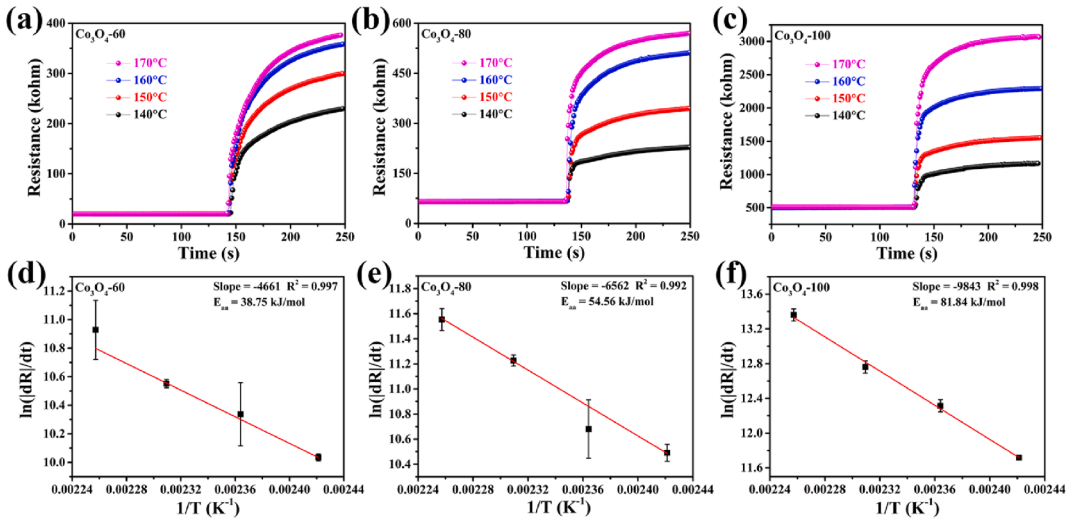

Fig. 7. Resistance changes for 100 ppm toluene and corresponding Arrhenius plots of the sensors based on (a, d) Co_3O_4-60, (b, e) Co_3O_4-80 and (c, f) Co_3O_4-100.

rate and Kelvin temperature (Fig. 7d-f). E_{aa} was calculated from the slopes of $|dR|/dt \sim 1/T$ in Fig. 7d-f. The E_{aa} of Co_3O_4-60 (38.75 kJ/mol) to toluene is smaller than that of Co_3O_4-80 (54.56 kJ/mol) and Co_3O_4-100 (81.84 kJ/mol). A lower E_{aa} indicates that less energy is required to trigger the sensing reaction. Thus, Co_3O_4-60 exhibits a high response with low optimal operating temperature in the detection of toluene. Correspondingly, the E_{aa} of Co_3O_4-60 (39.69 kJ/mol), Co_3O_4-80 (40.01 kJ/mol), and Co_3O_4-100 (49.89 kJ/mol) to triethylamine (as shown in Fig. S9) were calculated. Co_3O_4-80 and Co_3O_4-100 possessed higher E_{aa} to toluene than triethylamine. However, the E_{aa} of Co_3O_4-60 to toluene significantly reduced to a value comparable to that of triethylamine but slightly lower, indicating that the preferential affinity to toluene was tailored for Co_3O_4-60. Thus, Co_3O_4-60 exhibited superior sensing performance against triethylamine interference. The better selectivity resolution of Co_3O_4-60 originates from the various instinct properties of interference gases. It is possible that the effects of crystal facet on the interfering gases caused their different variation in operating temperature and gas response, which eventually caused an improvement in the selectivity resolution.

The gas-sensing performance of the Co_3O_4-60 gas sensor to toluene at 170 °C is shown in Fig. 8. Fig. 8a shows its response-recovery curve to 100 ppm toluene with a response time of 68 s and a recovery time of 81 s. While, as shown in Fig. S10, the Co_3O_4-80 (82 s) and the Co_3O_4-100 (153 s) exhibit longer recovery times than the Co_3O_4-60, which might be related to the re-formation process of chemisorbed oxygen [34]. It can be seen from Fig. 8b that the sensor's baseline resistance and gas response are basically stable during the consecutive detections of 100 ppm toluene, indicating its good repeatability. The gas responses to 100 ppm of possible interfering components are shown in Fig. 8c and Fig. S11, which reveals its good selectivity. Fig. 8d is the dynamic concentration gradient transient response to 1–100 ppm toluene. The relationship between response and gas concentration is plotted in Fig. 8e. The Co_3O_4-60 gas sensor has a detection limit of 1 ppm, with a gas response of 1.29. The corresponding linear-logarithmic relationship is established in the inset, with the linear equation $\mathrm{Log}(S-1) = 1.01 \times \mathrm{Log}(C) - 0.72$, $R^2 = 0.988$. As a result, the Co_3O_4-60 gas sensor is well suited for toluene detection in the concentration range of 1–100 ppm. Compared with the concentration gradient response-recovery curves of

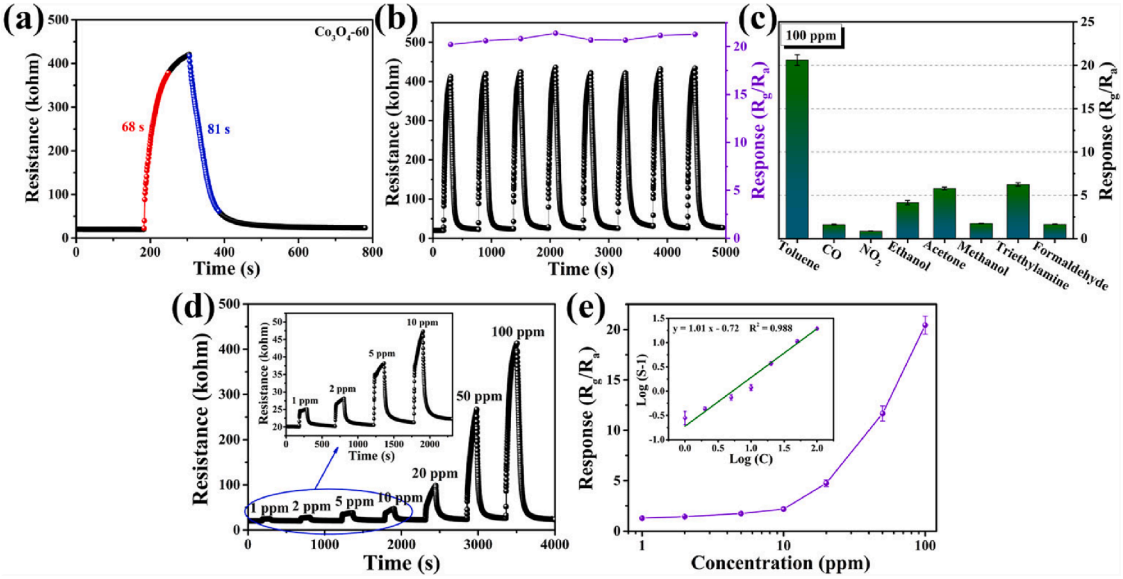

Fig. 8. (a) Dynamic response-recovery curve and (b) consecutive response-recovery curves to 100 ppm toluene and relevant responses for each cycle; (c) responses to 100 ppm of various gases; (d) concentration gradient response-recovery curves and (e) corresponding plots of response and concentration of Co_3O_4-60 gas sensor at 170 °C.

Co_3O_4-80 and Co_3O_4-100 gas sensors (Fig. S12), the Co_3O_4-60 gas sensor has the highest response at all concentrations tested. We summarized recent reports of Co_3O_4 gas sensors for the detection of toluene in Table S2 [35–39]. The gas sensor based on Co_3O_4-60 has superior sensitivity to toluene at lower operating temperature, reflecting our contribution.

Fig. 9a shows the dynamic response-recovery curves of Co_3O_4-60 gas sensor to 100 ppm toluene in several humidity levels (30RH%, 50RH%, 70RH%, 90RH%). And their corresponding baseline resistance and gas responses are exhibited in Fig. 9b. The baseline resistance increased, and the gas response decreased as the humidity increased during the test. This was attributed to the reaction of H_2O molecules with chemisorbed oxygen, which forms hydroxyl groups on the surface of the material, impeding charge and mass transfer and weakening the gas-sensing reaction [40]. Long-term stability is also an important metric for evaluating sensor performance. During the three consecutive weeks of testing, as shown in Fig. 10, although the baseline resistance rose significantly, the overall response was stable with only a tiny drop. Recently, humidity drift compensations and long-term drift compensation have been used in gas sensors [40–42] and are expected to attenuate adverse effects in practical applications.

3.3. Gas sensing mechanism

The sensing mechanism in this work is mainly derived from the resistance change driven by surface chemistry. In air, due to the higher electron affinity of O_2 molecules, they can extract electrons from the conduction band of the material surface and form chemisorbed oxygen (O^-) while forming a hole accumulation layer (HAL) in the surface of Co_3O_4, resulting in lower resistance. When the sensors are exposed to toluene, toluene molecules will react with the chemisorbed oxygen to generate CO_2 and H_2O while releasing the electrons back to the material surface. The return of electrons reduces the thickness of HAL, causing the sensor resistance to rising. The above reaction processes were shown in Fig. 11 and expressed as equations (2)-(4) [35]:

$$O_{2(gas)} + e^- \rightarrow O^-_{2(ads)} \quad (2)$$

$$O^-_{2(ads)} + e^- \rightarrow 2O^-_{(ads)} \quad (3)$$

$$C_7H_8 + 18O^-_{(ads)} \rightarrow 7CO_2 + 4H_2O + 18e^- \quad (4)$$

The gas sensor based on Co_3O_4-60 exhibited excellent toluene detection performance. Its uniform nanosheet structure, equal mesoporous distribution, and sufficient exposed area of crystal facets {1 1 1} are favorable for gas diffusion and adsorption. Meanwhile, Co_3O_4-60 with exposed crystal facets {1 1 1} increases the content of chemisorbed oxygen on the material surface and exposes more reaction sites for gas detection. On the other hand, the catalytic effect originating from the abundant Co^{2+} and the lower apparent activation energy synergistically promote the gas-sensing reaction of Co_3O_4-60. Besides, more surface chemisorbed oxygen captures more electrons from Co_3O_4-60. It forms a thicker HAL, which, combined with the bigger crystallite size, ultimately reduces the baseline resistance. According to the definition of gas response in this work, low baseline resistance and significant resistance change owing to rich reaction sites would corporately determine the superior response. In summary, the design of exposed crystal facets {1 1 1} regulated electrical and catalytical properties and ultimately improved the sensing performance.

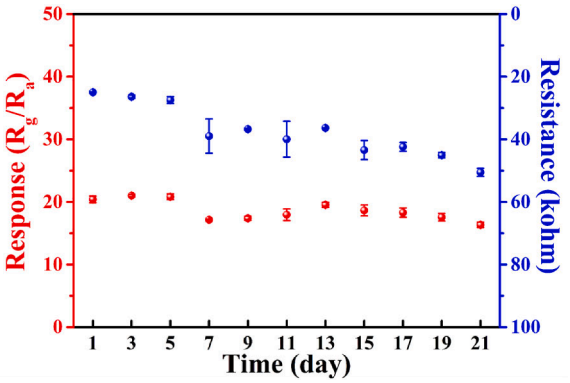

Fig. 10. The response and baseline resistance of Co_3O_4-60 gas sensor in 21 days.

4. Conclusion

In summary, Co_3O_4 mesoporous nanosheets with exposed {1 1 1} or {1 1 2} crystal facets were prepared by controlling the intermedia of CoOOH at different reflux temperatures. The nanosheet structure and uniformly distributed mesoporous channels benefit the exposed area of ideal crystal facets and the diffusion of gases. The gas sensor based on Co_3O_4-60 with exposed Co^{2+}-rich {1 1 1} facets exhibited the best gas response to toluene due to its higher Co^{2+} content, more chemisorbed oxygen, lower apparent activation energy, and lower baseline resistance. The Co_3O_4-60 gas sensor had a response of 20.6 for 100 ppm toluene with a detection limit of 1 ppm and good repeatability at the optimal operating temperature of 170 °C. This work proves that crystal facet engineering is a promising strategy and provides a reference for further improving the gas-sensing properties of materials.

CRediT authorship contribution statement

Dehao Kong: Conceptualization, Methodology, Writing – original draft, Formal analysis, Validation. **Weirong Zhou:** Methodology, Investigation, Visualization. **Jiayin Han:** Validation, Visualization.

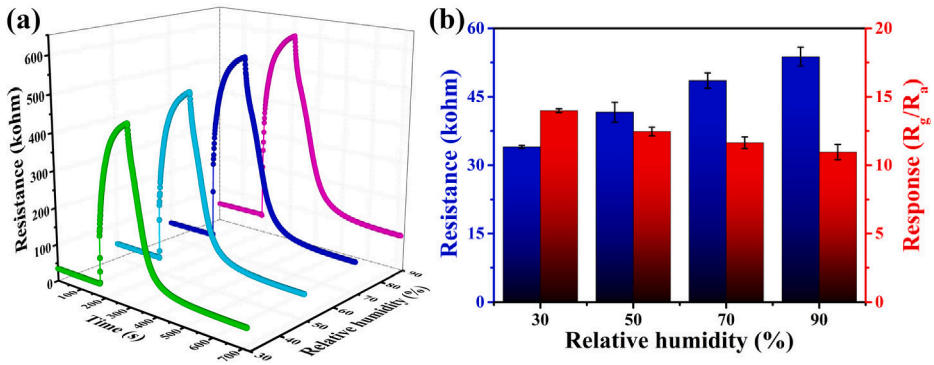

Fig. 9. (a) Dynamic response-recovery curves, (b) baseline resistances and gas responses of Co_3O_4-60 gas sensor for 100 ppm toluene at four humidity levels at 170 °C.

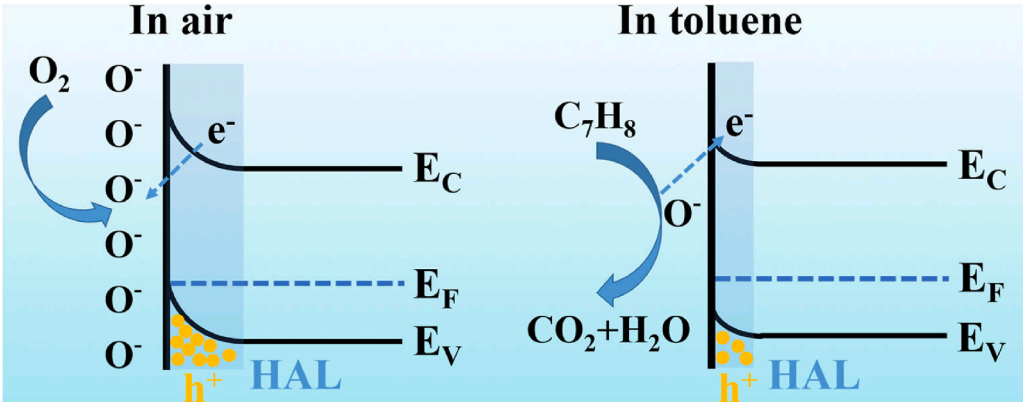

Fig. 11. Schematic diagram of the toluene detection mechanism of the sensors.

Yubing Gao: Methodology, Validation. **Yuan Gao:** Conceptualization, Methodology, Writing – review & editing, Project administration, Funding acquisition. **Liupeng Zhao:** Investigation. **Peng Sun:** Conceptualization, Project administration, Supervision, Funding acquisition. **Geyu Lu:** Writing – review & editing, Supervision, Funding acquisition.

Declaration of Competing Interest

The authors declare that they have no known competing financial interests or personal relationships that could have appeared to influence the work reported in this paper.

Data availability

Data will be made available on request.

Acknowledgments

This work was supported by the National Natural Science Foundation of China (62171196), Natural Science Foundation of Jilin Province (20200201289JC), National Key Research and Development Program of China (No. 2021YFB3201300), Science and Technology Project of Jilin Provincial Department of Education (JJKH20200982KJ), and China Postdoctoral Science Foundation (2019T120238, 2018M640282).

Appendix A. Supplementary data

Supplementary data to this article can be found online at https://doi.org/10.1016/j.apsusc.2023.156714.

References

[1] K.B. Kim, S.-Y. Jeong, T.-H. Kim, et al., Methylbenzene sensors using Ti-doped NiO multiroom spheres: Versatile tunability on selectivity, response, sensitivity, and detection limit, Sens. Actuators, B 308 (2020), 127730.
[2] A. Mirzaei, J.-H. Kim, H.W. Kim, et al., Resistive-based gas sensors for detection of benzene, toluene and xylene (BTX) gases: a review, J. Mater. Chem. C 6 (2018) 4342–4370.
[3] G. Gregis, S. Schaefer, J.-B. Sanchez, et al., Characterization of materials toward toluene traces detection for air quality monitoring and lung cancer diagnosis, Mater. Chem. Phys 192 (2017) 374–382.
[4] D. Zappa, V. Galstyan, N. Kaur, et al., "Metal oxide-based heterostructures for gas sensors"-A review, Anal. Chim. Acta 1039 (2018) 1–23.
[5] Z. Cao, Y. Ge, W. Wang, et al., Chemical Discrimination of Benzene Series and Molecular Recognition of the Sensing Process over Ti-Doped Co_3O_4, ACS Sens. 7 (2022) 1757–1765.
[6] H. Liu, Z. Wang, G. Cao, et al., Construction of hollow NiO/ZnO p-n heterostructure for ultrahigh performance toluene gas sensor, Mater. Sci. Semicond. Process. 141 (2022), 106435.
[7] X. Liu, X. Duan, C. Zhang, et al., Improvement toluene detection of gas sensors based on flower-like porous indium oxide nanosheets, J. Alloys Compd. 897 (2022), 163222.
[8] X. Liu, J. Zhang, S. Wu, et al., Single crystal α-Fe_2O_3 with exposed {104} facets for high performance gas sensor applications, RSC Adv. 2 (2012) 6178–6184.
[9] T. Yu, X. Li, B. Chen, et al., Enhanced Gas Sensing Performance of rGO Wrapped Crystal Facet-Controlled Co_3O_4 Nanocomposite Heterostructures, J. Phys. Chem. C 126 (2022) 4879–4888.
[10] J. Xu, Z. Xue, N. Qin, et al., The crystal facet-dependent gas sensing properties of ZnO nanosheets: Experimental and computational study, Sens. Actuators, B 242 (2017) 148–157.
[11] J. Zhao, Z. Tang, F. Dong, et al., Controlled porous hollow Co_3O_4 polyhedral nanocages derived from metal-organic frameworks (MOFs) for toluene catalytic oxidation, Mol. Catal. 463 (2019) 77–86.
[12] J. Deng, W. Song, L. Chen, et al., The effect of oxygen vacancies and water on HCHO catalytic oxidation over Co_3O_4 catalyst: A combination of density functional theory and microkinetic study, Chem. Eng. J. 355 (2019) 540–550.
[13] Q. Ren, S. Mo, J. Fan, et al., Enhancing catalytic toluene oxidation over MnO_2@Co_3O_4 by constructing a coupled interface, Chin. J. Catal. 41 (2020) 1873–1883.
[14] J. Xiao, Q. Kuang, S. Yang, et al., Surface structure dependent electrocatalytic activity of Co_3O_4 anchored on graphene sheets toward oxygen reduction reaction, Sci. Rep. 3 (2013) 2300.
[15] H. Liu, H. He, L. Chen, et al., Flower-like Co_3O_4 sensor with rich oxygen vacancy defects for enhancing room temperature NO_x sensing performances, J. Alloys Compd. 868 (2021), 159180.
[16] T. Zhou, T. Zhang, J. Deng, et al., P-type Co_3O_4 nanomaterials-based gas sensor: Preparation and acetone sensing performance, Sens. Actuators, B 242 (2017) 369–377.
[17] S. Zhao, T. Li, J. Lin, et al., Engineering Co^{3+}-rich crystal planes on Co_3O_4 hexagonal nanosheets for CO and hydrocarbons oxidation with enhanced catalytic activity and water resistance, Chem. Eng. J. 420 (2021), 130448.
[18] T. Pauporté, L. Mendoza, M. Cassir, et al., Direct Low-Temperature Deposition of Crystallized CoOOH Films by Potentiostatic Electrolysis, J. Electrochem. Soc. 152 (2005) C49–C53.
[19] J. Yang, H.W. Liu, W.N. Martens, et al., Synthesis and Characterization of Cobalt Hydroxide, Cobalt Oxyhydroxide, and Cobalt Oxide Nanodiscs, J. Phys. Chem. C 114 (2010) 111–119.
[20] C.D. Dimitrakopoulos, P.R.L. Malenfant, Organic Thin Film Transistors for Large Area Electronics, Adv. Mater. 14 (2002) 99–117.
[21] X. Liu, L. Zhang, Y. Zheng, et al., Uncovering the Effect of Lattice Strain and Oxygen Deficiency on Electrocatalytic Activity of Perovskite Cobaltite Thin Films, Adv. Sci. 6 (2019) 1801898.
[22] K. Qian, Y. Yan, S. Xi, et al., Elucidating the Strain-Vacancy-Activity Relationship on Structurally Deformed Co@CoO Nanosheets for Aqueous Phase Reforming of Formaldehyde, Small 17 (2021) 2102970.
[23] X. Wang, X. Li, J. Mu, et al., Oxygen Vacancy-rich Porous Co_3O_4 Nanosheets toward Boosted NO Reduction by CO and CO Oxidation: Insights into the Structure-Activity Relationship and Performance Enhancement Mechanism, ACS Appl. Mater. Interfaces 11 (2019) 41988–41999.
[24] C. Gao, Q. Meng, K. Zhao, et al., Co_3O_4 Hexagonal Platelets with Controllable Facets Enabling Highly Efficient Visible-Light Photocatalytic Reduction of CO_2, Adv. Mater. 28 (2016) 6485–6490.
[25] X. Han, G. He, Y. He, et al., Engineering Catalytic Active Sites on Cobalt Oxide Surface for Enhanced Oxygen Electrocatalysis, Adv. Energy Mater. 8 (2017) 1702222.
[26] B. Qiu, C. Wang, N. Zhang, et al., CeO_2-Induced Interfacial Co^{2+} Octahedral Sites and Oxygen Vacancies for Water Oxidation, ACS Catal. 9 (2019) 6484–6490.
[27] T. Cai, H. Huang, W. Deng, et al., Catalytic combustion of 1,2-dichlorobenzene at low temperature over Mn-modified Co_3O_4 catalysts, Appl. Catal., B 166-167 (2015) 393–405.
[28] Z. Xiao, Y. Wang, Y.-C. Huang, et al., Filling the oxygen vacancies in Co_3O_4 with phosphorus: an ultra-efficient electrocatalyst for overall water splitting, Energy Environ. Sci. 10 (2017) 2563–2569.
[29] H. Yu, C. Guo, X. Zhang, et al., Tailoring Oxygen Vacancy of Co_3O_4 Microcubes by Annealing $Co_3[Co(CN)_6]_2$ Template in Air for Ultrasensitive Humidity Mapping, Small Struct. 3 (2022) 2100166.

[30] H. Zhu, X. Song, X. Han, et al., Co_3O_4 Nanosheets Preferentially Growing (220) Facet with a Large Amount of Surface Chemisorbed Oxygen for Efficient Oxidation of Elemental Mercury from Flue Gas, Environ. Sci. Technol. 54 (2020) 8601–8611.
[31] X. Wang, X. Zhang, Y. Wei, et al., In situ grown Co_3O_4 nanosheets in the interlayer space of g-C_3N_4 for efficient removal of Hg^0 from flue gas, Fuel 324 (2022), 124660.
[32] J. Yang, W. Han, J. Ma, et al., Sn doping effect on NiO hollow nanofibers based gas sensors about the humidity dependence for triethylamine detection, Sens. Actuators, B 340 (2021), 129971.
[33] F. Gu, Y. Cui, D. Han, et al., Atomically dispersed Pt (II) on WO_3 for highly selective sensing and catalytic oxidation of triethylamine, Appl. Catal., B 256 (2019) 117809.
[34] J. Li, Q. Ding, X. Mo, et al., A highly stable and sensitive ethanol sensor based on Ru-decorated 1D WO_3 nanowires, RSC Adv. 11 (2021) 39130–39141.
[35] R. Zhang, S. Gao, T. Zhou, et al., Facile preparation of hierarchical structure based on p-type Co_3O_4 as toluene detecting sensor, Appl. Surf. Sci. 503 (2020), 144167.
[36] J. Cao, S. Wang, X. Zhao, et al., Facile synthesis and enhanced toluene gas sensing performances of Co_3O_4 hollow nanosheets, Mater. Lett. 263 (2020), 127215.
[37] L. Wang, S.Y. Song, B. Hong, et al., Highly improved toluene gas-sensing performance of mesoporous Co_3O_4 nanowires and physical mechanism, Mater. Res. Bull. 140 (2021), 111329.
[38] J. Cao, S. Wang, J. Li, et al., Porous nanosheets assembled Co_3O_4 hierarchical architectures for enhanced BTX (Benzene, Toluene and Xylene) gas detection, Sens. Actuators, B 315 (2020), 128120.
[39] H.M. Jeong, J.H. Kim, S.Y. Jeong, et al., Co_3O_4-SnO_2 Hollow Heteronanostructures: Facile Control of Gas Selectivity by Compositional Tuning of Sensing Materials via Galvanic Replacement, ACS Appl. Mater. Interfaces 8 (2016) 7877–7883.
[40] M. Yan, Y. Wu, Z. Hua, et al., Humidity compensation based on power-law response for MOS sensors to VOCs, Sens. Actuators, B 334 (2021), 129601.
[41] L. Yueyue, S. Siqi, W. Yilin, et al., $CsPbBr_3$ quantum dots enhanced ZnO sensing to NO_2 at room temperature, Sens. Actuators, B 368 (2022), 132189.
[42] X. Dong, S. Han, A. Wang, et al., Online Inertial Machine Learning for Sensor Array Long-Term Drift Compensation, Chemosensors 9 (2021) 353.